

Article

Numerical Investigation on the Electroslag Remelting of High Carbon Martensitic Stainless Steels

Xingyu Liu , Guotao Zhou, Yangyang Shen, Wei Yan * and Jing Li

State Key Laboratory of Advanced Metallurgy, University of Science and Technology Beijing, Beijing 100083, China

* Correspondence: weiyang@ustb.edu.cn

Abstract: Control of solidification structure and segregation is crucial to improve the service performance of high carbon martensitic stainless steels. Design of the electroslag remelting (ESR) process based on the essential parameters of melting rate, filling ratio, and slag thickness is a precondition to achieve optimal control of solidification structure and segregation of the steels. However, there is still a lack of coupled works giving deep insight into the overall effect of the parameters on the expected control. With this background, a 2D numerical model was established to probe into the effect of process parameters. The results showed that: (1) With the increase of melting rate from 90 kg/h to 180 kg/h, the molten metal pool depth increased by about 4 cm. Meanwhile, the center LST, PDAS, and SDAS increased by about 450 s, 100 μm , and 12 μm . The segregation index of C and Cr increased by about 0.15 and 0.09. (2) As the filling ratio increased from 0.16 to 0.43, the depth of the metal pool decreased by about 4.5 cm, LST and SDAS received a slight increase of about 41 s and less than 5 μm , but PDAS had little change. The segregation index of C had an increase of about 0.03, but the segregation index of Cr demonstrated tiny changes. (3) As the slag thickness increased from 0.08 to 0.14 m, the metal pool depth presented a first increase of about 1 cm and then a slight decrease. The center LST, PDAS, and SDAS first increased by 148 s, 30 μm , and 4 μm and then decreased slightly. The changes of the segregation index of C and Cr presented a similar tendency than that of LST, but the changes are extremely small. (4) A low melting rate less than 120 kg/h, a filling ratio of about 0.23–0.33, and a slag thickness of 0.08–0.10 m were appropriate to obtain good performance for ESR of high carbon stainless steels in this study.



Citation: Liu, X.; Zhou, G.; Shen, Y.; Yan, W.; Li, J. Numerical Investigation on the Electroslag Remelting of High Carbon Martensitic Stainless Steels. *Metals* **2023**, *13*, 482. <https://doi.org/10.3390/met13030482>

Academic Editor: Antonio Mateo

Received: 2 January 2023

Revised: 16 February 2023

Accepted: 23 February 2023

Published: 26 February 2023



Copyright: © 2023 by the authors. Licensee MDPI, Basel, Switzerland. This article is an open access article distributed under the terms and conditions of the Creative Commons Attribution (CC BY) license (<https://creativecommons.org/licenses/by/4.0/>).

Keywords: electroslag remelting; numerical simulation; process parameters; metal pool; solidification; high carbon martensitic stainless steels

1. Introduction

High carbon martensitic stainless steels are broadly used in production of high-grade knives and structural components because of their high hardness, strength, abrasive resistance, and corrosion resistance. The essential production process of these special steels generally includes ingot casting [1], continuous casting [2,3], and ESR [4]. The steel ingots produced through these processes have critical influence on the final product quality.

Among these processes, ESR has a high advantage in controlling solidification structure and chemical refining of high carbon martensitic stainless steels. During the ESR process, the melting of the electrode and the solidification of molten metal take place simultaneously. On the one hand, the metal droplets continuously supply liquid metal from the electrode to the molten metal pool. On the other hand, the metal in the mould is strongly cooled by the water-cooling bottom and wall, and thus solidification takes place in the shallow molten pool. Since the solidification starts from the mould bottom, shrinkage of the metal can be compensated by the molten pool, and the gas and inclusions in the liquid metal are easy to float up; hence, the microstructure of the ESR ingot is dense and uniform compared to the conventional casting ingot [5].

In order to ensure good service performance, it is necessary to improve the solidification structure and meanwhile control the solute segregation as well as the resulting carbide of high carbon martensitic stainless steels. Considering the advantages of the ESR process, the ESR process is employed to produce a steel ingot with high requirement for quality. The coordination of ESR process parameters is an essential precondition for good ingot quality. In the ESR process, the molten pool is an important zone, which deeply influences the heat transfer and solute transport, and thus influences the solidification structure and segregation. The melting rate of the electrode is a performance of the electrical current of the ESR process, which further affects the slag temperature and depth of the molten pool [6]. The filling ratio of the electrode is defined as area ratio of electrode to mould, which affects the electrical current path in the slag region and thus affects the heat transfer to the metal/slag interface and the molten pool characteristics [7]. The slag generates heat to melt the electrode, so the change of slag thickness may affect the molten pool shape [8]. Accordingly, the melting rate, filling ratio, and slag thickness are three key parameters affecting the ESR solidification process. Liu et al. [9] reported the effect of melting rate characterized by current on an ESR of low carbon dual alloy ingot based on laboratory-scale experiments and found that less dendrite segregation and finer precipitates could be achieved at low current. Wang et al. [10] conducted a similar study on Ni transport in ESR dual alloy ingot and found that the rise of current increased the metal pool depth and the segregation of Ni. In the above studies, the steels are low carbon and low alloy steel grades, and the segregation is weak compared to high carbon martensitic stainless steels in the present study. Wang et al. [11] reported the solute segregation and precipitation of the primary carbides in H13 ESR ingot and found primary carbides mainly distributed in the interdendritic region where the solutes are enriched. But he did not offer the suggestion to control enrichment of solutes. Chen et al. [6] reported the effect of melting rate on the surface quality and solidification structure of Mn18Cr18N hollow ESR ingot and obtained technical parameters to achieve good surface quality; its difference from conventional ESR process is that the ESR ingot is hollow, and the ingot is withdrawn during ESR. This cannot provide reference for control of the structure and segregation in the center zone. Du et al. [12] compared the effect of electroslag remelting-continuous rapid solidification (ESR-CRS) and conventional ESR on carbides in GCr15 steel and found that the ESR-CRS process had a stronger capacity to suppress segregation and refine the microstructure due to intensive cooling. But this is difficult to achieve in the conventional ESR process. It can be found from the aforementioned studies that most experiments focus on the effect of melting rate and different ESR processes. Due to the limitations of safety and facility, few experimental studies on molten pool characteristics, filling ratio, and slag thickness can be found, especially for ESR of high carbon martensitic stainless steels.

ESR process is a complicated “black box”, so it is difficult to know more about the temperature and element distributions, as well as the molten slag and steel flow patterns during solidification through experiment. It is also time-consuming and has high experimental trial costs to learn about the structures and how to optimize the ESR process. However, it is necessary to learn about the effects of those parameters such as melting rate, filling ratio, and slag thickness on the solidification process and structure, as well as solute segregation, to optimize the ESR process. Wang et al. [13,14] simulated the ESR process to predict the macrosegregation of Ni in 201 stainless steels using constant parameters. But he did not investigate the effect of ESR parameters such as melting rate and slag thickness on segregation and structure of ESR ingots. Li et al. [15] investigated the effects of the current frequency, electrode immersion depth, and slag thickness on the electric and magnetic characteristics as well as Joule heating in slag through a 3D finite element model. But the temperature distribution, solidification structure, and solute segregation were not presented. Weber et al. [16] constructed a 2D transient-state numerical model to study the effect of electrode fill ratio on pool profile and Joule heating during the ESR process of Ni-based alloy Nimonic 80A. Nevertheless, structure and element segregation were not reported in his study. Huang et al. [17] developed a comprehensive transient

model to study the effect of electrode rotation on the evolution of metal pool profiles and the solidification quality of H13 ESR ingots. The results showed that the temperature distributions became uniform and the pool profiles became flat at high rotating speed, but the local solidification time and the secondary dendrite arm spacing increased. The solute segregation was not reported.

As discussed above, few experimental studies reported the effect of filling ratio and slag thickness on the molten pool characteristics, structure, and segregation during the ESR process. Modelling studies compensated some deficiencies of experimental studies, but there is still a lack of coupled works concerning the overall effect of process parameters such as melting rate, filling ratio, and slag thickness on the ESR solidification process, especially for the high-carbon high-alloy and segregation-susceptible steel in the present study, and the control of the solidification process and segregation is crucial for these steels. In order to deeply and thoroughly understand the solidification process and obtain quantitative information in ESR of high carbon martensitic stainless steels for process design and optimization, the present study on temperature and flow field of metal and slag pools, solidification characteristics, and element segregation was conducted through a numerical simulation method concerning the melting rate, filling ratio, and slag thickness.

2. Numerical Simulation

2.1. Assumptions

Melting of the electrode and the solidification of molten metal take place simultaneously during ESR. In order to simulate these two processes, the finite element analysis software Melt-Flow 3.1 was employed to establish the model of ESR in the present study. The calculation range starts from top surface of slag and finishes at bottom of remelted steel ingot. The top surface of slag is viewed as the reference surface. For a round ESR mould, the following assumptions are made to simplify the calculation process [18–21]:

- (1) The model is assumed to be axisymmetric.
- (2) The electrode/slag and the slag/metal interfaces are assumed to be flat.
- (3) The model calculation is based on the steady state conditions.
- (4) A frame of reference attached to the electrode/slag interface is used for reference surface, where the slag is stationary, but the ingot grows downwards.
- (5) The electrode is not included in the computational domain because the thermal and the electromagnetic effects within the electrode are limited to a very thin boundary layer.
- (6) The slag/metal interface is treated implicitly using a unified domain containing both the slag and the ingot.
- (7) The solidification shrinkage of slag skin with decrease of temperature is neglected, and there is no air gap between slag skin and mould wall.

2.2. Electromagnetic Phenomena

The electromagnetic field is an essential physical phenomenon of the ESR process. The electromagnetic field could be expressed through Maxwell's equations [18,21,22]:

Magnetic diffusion:

$$\nabla \cdot \left(\frac{1}{\sigma} \nabla (\hat{H}_\theta e_\theta) \right) = j\mu_0\omega\hat{H}_\theta \quad (1)$$

Magnetic flux density:

$$\hat{B}_\theta = \mu_0\hat{H}_\theta \quad (2)$$

Current density:

$$\hat{\mathbf{j}} = \nabla \times (\hat{H}_\theta e_\theta) \quad (3)$$

Lorentz force:

$$\mathbf{F}_L = \text{Re} \left(\frac{1}{2} \hat{\mathbf{j}} \times \text{conjugate}(\hat{\mathbf{B}}) \right) \quad (4)$$

Joule heating:

$$S_J = \frac{1}{2\sigma} \hat{\mathbf{j}} \times \text{conjugate}(\hat{\mathbf{j}}) \quad (5)$$

The radial current on the slag/electrode interface and ingot bottom are assumed to be zero during the ESR process. The boundary conditions of the electromagnetic field could be expressed as follows [18]:

Slag/electrode interface and ingot bottom:

$$\frac{\partial \hat{H}_\theta}{\partial x} = 0 \quad (6)$$

Exposed slag surface:

$$\hat{H}_\theta(r) = \frac{1}{2\pi r} \hat{\mathbf{I}} \quad (7)$$

Circumferential surface of ESR ingot:

$$\hat{H}_\theta(r) = \frac{1}{2\pi R_{\text{ingot}}} \hat{\mathbf{I}} \quad (8)$$

2.3. Flow Field

The metal pool is under the slag pool during the ESR process. Flow of molten slag and metal is controlled with the buoyancy force and Lorentz force. The macroscopic flow in the metal pool and slag pool can be controlled using the mass conservation equation and the momentum conservation equation. The time-averaged form of the Navier–Stokes equation is employed to describe the flow field [21,23].

Mass conservation:

$$\frac{\partial \rho}{\partial t} + \nabla \cdot (\rho \mathbf{u}) = 0 \quad (9)$$

Momentum conservation:

$$\frac{\partial (\rho \mathbf{u})}{\partial t} + \nabla \cdot (\rho \mathbf{u} \otimes \mathbf{u}) = -\nabla P + \nabla \cdot (\mu_{eff} (\nabla \mathbf{u} + \nabla \mathbf{u}^T)) - \rho \mathbf{g} + \mathbf{F}_L \quad (10)$$

The flow in the slag and metal pool is supposed to be weakly turbulent according to the ESR process conditions and ingot size [24]. And the turbulent mixing in the slag may be changed obviously. A k - ε turbulence model is employed to calculate the effect of turbulent mixing on the flow and the temperature fields. The turbulent viscosity could be calculated through turbulent kinetic energy and turbulent dissipation. Then, the turbulent conductivity could be calculated based on the turbulent viscosity using Reynold's analogy.

Turbulent kinetic energy [18,23]:

$$\nabla \cdot (\rho \mu k) = \nabla \cdot \left(\frac{\mu_t}{\sigma_k} \nabla k \right) + \mu_t G - \rho \varepsilon \quad (11)$$

Turbulent dissipation [18,23]:

$$\nabla \cdot (\rho \mu \varepsilon) = \nabla \cdot \left(\frac{\mu_t}{\sigma_\varepsilon} \nabla \varepsilon \right) + (c_1 \mu_t G - c_2 \rho \varepsilon) \frac{\varepsilon}{k} \quad (12)$$

Turbulent viscosity [18,21,23,25]:

$$\mu_t = c_u \frac{\rho k^2}{\varepsilon} \quad (13)$$

Turbulent conductivity [18,21]:

$$\frac{k_t}{C_p} = \frac{\mu_t}{Pr_t} \quad (14)$$

The previous governing equations are subjected to the following boundary conditions. A no-slip boundary condition is imposed on the region of the mold boundary where the molten slag and metal are in contact with the mould. On the exposed top surface of the slag and electrode/slag interface, the shearing stress is zero for the free top surface of the slag and electrode/slag interface. In the region of ESR ingot, the macrolevel flow is supposed to be absent below the liquid fraction, and it corresponds to the solid/liquid interface in the flow calculation [18].

Top surface:

$$\frac{\partial u_y}{\partial x} = 0 \quad (15)$$

Mould surface:

$$u = 0 \quad (16)$$

Due to the employment of the k - ε turbulence model, enhanced wall functions are used to calculate the turbulent kinetic energy, turbulent dissipation, shear stress, and heat flux on all the solid surfaces and the molten pool boundary. In the solidified zone, k and ε are set as zero. At the liquid/solid surface, a normal gradient of zero is imposed for both k and ε [16,18].

Mould surface and molten pool boundary:

$$\frac{\partial k}{\partial y} = 0 \quad (17)$$

$$\varepsilon = \frac{(C_u k^2)^{\frac{3}{2}}}{ky} \quad (18)$$

Top slag surface:

$$\frac{\partial k}{\partial y} = 0 \quad (19)$$

$$\frac{\partial \varepsilon}{\partial y} = 0 \quad (20)$$

Top surface of metal pool:

$$k = cu_{in}^2 \quad (21)$$

$$\varepsilon = \frac{k^{\frac{3}{2}}}{l_f R_0} \quad (22)$$

2.4. Energy Conservation and Solidification

The temperature distributions in the slag and molten pool and ingot are governed by the following energy conservation equation. Where Joule heating is a heating source term of the equation generated by the electric current, it dominates the heat in the slag pool. In the molten pool, the released latent heat during metal solidification is also a heating source term. It is related to the local liquid fraction f_1 which can be obtained through the functional relationship with the featured temperature of metal.

Energy conservation [21]:

$$\frac{\partial(\rho uh)}{\partial t} + \nabla \cdot (\rho uh) = \nabla \cdot (k_{eff} \nabla T) - \left(\frac{\partial(\rho \Delta H)}{\partial t} + \nabla \cdot (\rho u \Delta H) \right) \quad (23)$$

Sensible enthalpy [13]:

$$h = h_{ref} + \int_{T_{ref}}^T C_p dT \quad (24)$$

Latent heat [21]:

$$\Delta H = f(T)L, T_{sol} \leq T \leq T_{liq} \quad (25)$$

Liquid fraction [26]:

$$f_L = \begin{cases} 0 & T \leq T_{sol} \\ \frac{T - T_{sol}}{T_{liq} - T_{sol}} & T_{sol} < T \leq T_{liq} \\ 1 & T > T_{sol} \end{cases} \quad (26)$$

The local solidification time (LST) is defined as the required time for a metal volume to cool from the liquidus temperature to the solidus temperature, which reveals the residence time of metal volume in the mushy zone. The thermal history of the solidified ESR ingot obtained based on the energy conservation is used to calculate LST. The primary and second dendrite arm spacings could be also calculated using the following equations based on the thermal history of solidification of the ESR ingot [27,28].

Local solidification time:

$$LST = \frac{T_{liq} - T_{sol}}{G_L R} \quad (27)$$

Primary dendrite arm spacing (PDAS):

$$\lambda_1 = \frac{m_1}{(G_L R)^{n_1}} \quad (28)$$

Secondary dendrite arm spacing (SDAS):

$$\lambda_2 = \frac{m_2}{(G_L R)^{n_2}} \quad (29)$$

where m_1 , m_2 , n_1 , and n_2 are the constants determined by the alloy compositions. For a specific melting rate, the heat flux is supposed to be uniform at the slag/electrode interface. They are the energies heating the electrode from the inlet temperature to molten metal temperature and losing heat from the exposed slag surface, respectively. The temperature distribution could be determined using the following interactions on the ingot boundaries [18]:

Electrode/slag interface:

$$-k \frac{\partial T}{\partial x} = \frac{\dot{m} \left(L + \int_{T_{amb}}^{T_{liq}} C_p dT \right)}{A_{el}} \quad (30)$$

Exposed slag surface:

$$-k \frac{\partial T}{\partial x} = \varepsilon_e \sigma_b \left(T^4 - T_{sink}^4 \right) \quad (31)$$

2.5. Macrosegregation

The local concentrations of the alloying elements within the molten pool and the solid could be described by the convection–diffusion equations as follows [21].

Liquid region:

$$\frac{\partial(\rho c_i)}{\partial t} + \nabla \cdot (\rho u c_i) = \nabla \cdot \left(\left(\frac{\mu}{S c_i} + \frac{\mu_{turb}}{S c_{turb}} \right) \nabla c_i \right) + S_{i, sol-front} \quad (32)$$

Solid region:

$$\frac{\partial(\rho c_i)}{\partial t} + \frac{\partial(\rho u_{ingot} c_i)}{\partial x} = -S_{i, sol-front} \quad (33)$$

The governing equations are subjected to the following boundary conditions. For ingot top surface: the concentrations of the alloying elements in the metal flowing into the metal pool through the top surface of the ingot correspond to their concentrations at the melt front of the electrode. For pool boundary: the mass flux of an alloying element caused by selective rejection or absorption during this part of the solidification give rise to a source/sink in the liquid and a corresponding sink/source in the newly formed solid regions adjacent to the pool boundary. For each alloying element, this interface segregation flux is calculated from Scheil's equation with an equivalent segregation coefficient.

It should be noted that the present study employed a 2D axisymmetric model to simulate the ESR process such as in the works of Weber [16], Szekely [29], and Dong [30]. Compared with some 3D models reported by some researchers [13–15], the 2D model in this study shortens the calculation time and increases the efficiency, but it decreases the accuracy to a certain degree. Generally, an extension of the calculation zone along the axis can greatly reduce the discrepancy from 3D results. So, the full length of the ESR mould of more than one meter was used in the simulation in the present study. Another limitation is that 2D models cannot reveal the information along the normal direction. Accordingly, the information obtained from the symmetry plane was elaborated in this study.

2.6. Modelling Parameters

The electrode compositions of high carbon martensitic stainless steel for simulation are listed in Table 1. The steel properties including thermal conductivity, specific heat, and dynamic viscosity varied with temperature, and they were calculated using JMatPro 7.0, a universal material simulation and calculation software. The liquidus and solidus temperatures, as well as liquid and solid densities, were also calculated using JMatPro 7.0. A classical CaF₂-based ESR slag with the composition of 70CaF₂-15CaO-15Al₂O₃ was used during the simulation; the properties came from the Melt-Flow database. The main melting parameters are set based on an industrial trial, and are shown in Table 2.

Table 1. Compositions of ESR electrode.

| Element | C | Cr | Mo | V | Si | Mn | Co | Ni | Fe |
|--------------|-----|-------|------|------|------|------|------|------|---------|
| Content, wt% | 1.0 | 14.37 | 1.09 | 0.23 | 0.36 | 0.33 | 1.47 | 0.18 | Balance |

Table 2. Melting parameters used in simulation.

| Parameter | Value |
|-----------------------|------------------------|
| Mold diameter, m | 0.228 |
| Electrode diameter, m | 0.09, 0.11, 0.13, 0.15 |
| Ingot height, m | 1.2 |
| Slag height, m | 0.08, 0.10, 0.12, 0.14 |
| Melting rate, kg/h | 90, 120, 150, 180 |
| Current, kA | 3.75 |
| Frequency, Hz | 50 |

3. Results and Discussions

3.1. Temperature and Flow Field

3.1.1. Effect of Melting Rate on Temperature and Flow Field

Figure 1 demonstrates the temperature distribution, liquid fraction, and flow field at steady-state melting. It can be seen from the left half of each subfigure that the molten steel pool has a highest temperature at the top surface contacting the slag pool. This is because the electrode is first heated by slag, and it then melts into the molten pool, passing the slag pool, and subsequently solidifying. The slag is its unique physical heating source. The slag has a highest temperature zone at midradius position. In combination with the flow field appearing in the right half of subfigure, the highest temperature zone exactly corresponds

to the vortex created by the falling metal and Lorentz force, which is consistent with Wang's simulation results [31]. The decrease of temperature of the slag at the top, lateral and bottom zones is due to the stronger heat transfer to the ambient air, water-cooling wall, and molten pool. Moreover, it can be noticed that the slag closing to the center of the ingot has a descending temperature with an increasing melting rate. Figure 2 presents the change more intuitively through the change of highest slag temperature. The highest slag temperature decreases from about 2165 K to 2090 K when the melting rate increases from 90 kg/h to 180 kg/h. This is because more heat from the slag was consumed to melt the electrode to achieve a higher melting rate.

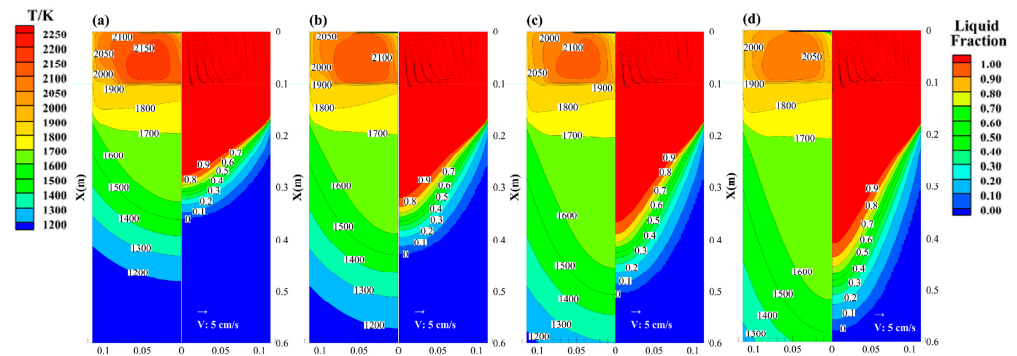


Figure 1. Temperature distribution (left of each figure) and liquid metal volume fraction distribution (right of each figure) at varying melting rates at end of steady state: (a) 90 kg/h, (b) 120 kg/h, (c) 150 kg/h, and (d) 180 kg/h.

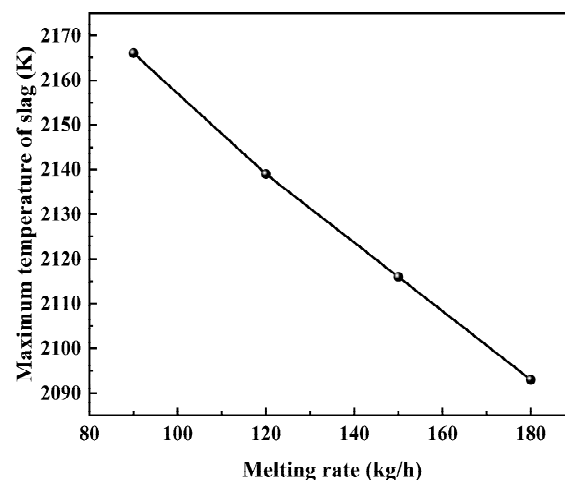


Figure 2. Effect of melting rate on maximum slag temperature.

As shown in the right half of Figure 1a–d, it can be noticed there is an anticlockwise vortex in the molten slag pool, but the vortex becomes clockwise in the molten steel pool. The length and direction of the arrow represent the magnitude and direction of flow velocity. It is obvious the flow of slag is stronger than the flow of molten steel. The largest flow velocity in the slag pool is far more than 5 cm/s, whereas the value of steel pool is much less than 5 cm/s according to the scale in the figure. A primary reason for this difference is the flow of slag is mainly controlled by the momentum of falling metal droplets and Lorentz force, but the flow of molten steel in the pool is mainly controlled by the thermal and solutal density differences, as well as an inward Lorentz force generated by the interaction between the self-induced magnetic field and the current, which would jointly drag or push the metal from the periphery to the bottom [31,32]. Lorentz force in slag pool is much larger than that in the molten steel pool especially for the case of higher melting rate. Thus, the

flow of slag is much stronger. Because increasing melting rate deepens the molten pool, the vortex area in the metal pool enlarges correspondingly.

The right half of Figure 1a–d also presents the profile of molten metal pool. It is easily found the metal pool gradually becomes deep “V” shape from shallow “U” shape with increasing melting rate. In order to clearly clarify the change of liquid metal pool depth ($f_L = 1.0$) and mushy zone width ($0 \leq f_L \leq 1.0$) with melting rate, Figure 3 plots the liquid metal pool depth and mushy zone width along radical direction. As shown in the figure, the liquid metal pool depth and mushy zone width present different rise with increase of melting rate from 90 kg/h to 180 kg/h, this can be contributed to the weaker cooling intensity in the center where solidification is difficult due to the increasing amount of central liquid metal. Generally, a shallow and flat liquid metal molten pool is expected to be formed during ESR process to obtain uniform and compact structures. The deep molten pool would accelerate the dendrite to grow toward the center, which increases the potential of bridging in the ingot center, resulting in the shrinkage defect. So, the growth direction of the columnar grains in the ESR ingot was usually expected to be less than 45° with respect to the rising direction of molten pool [33,34]. Moreover, the wider mushy zone indicates lower temperature gradient, which is not beneficial for formation of fine grain structures.

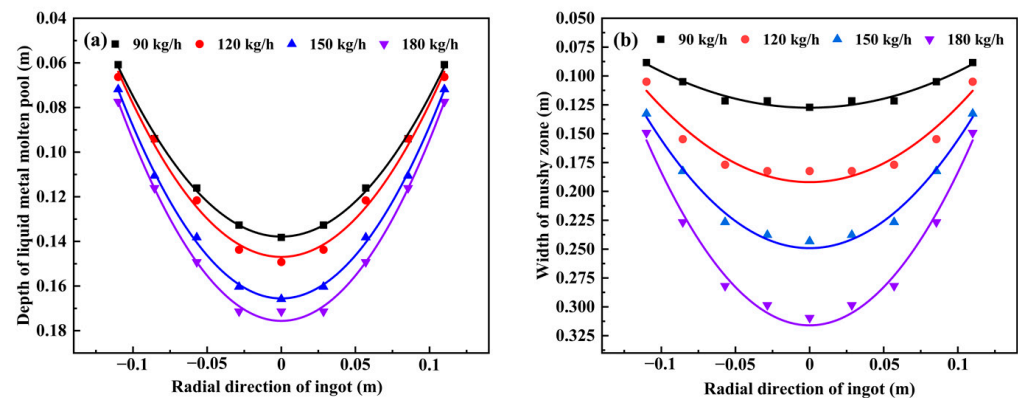


Figure 3. Change of metal pool depth (a) and mushy zone width (b) along radical direction at varying melting rates.

3.1.2. Effect of Filling Ratio on Temperature and Flow Field

Figure A1a–d illustrates the temperature and flow field with varying filling ratio. The left half of each figure illustrates the temperature field, the right half of each figure illustrates the flow field and liquid fraction contour. It can be observed the temperature of slag and liquid steel closing to the slag increases with rise of filling ratio. In combination with Figure 4, the maximum slag temperature and liquid steel temperature increase by more 200 K, respectively. Wang et al. [35] reported the similar temperature change based on the ESR of Q235 steel with vibrating electrode. Meanwhile, the area of high temperature zone of slag pool enlarges, both areas of the high temperature zone (above 1800 K) and middle temperature zone (1600–1700 K) of metal pool also enlarge. This may cause the ununiform temperature distribution in slag and metal pool. A possible reason is the increase of filling ratio reduces the exposed area of slag to open air atmosphere, resulting in the reduction of the heat loss. Moreover, increasing filling ratio prolongs the passing distance of electric current in slag, and thus creating more heating. The increase of slag temperature will transfer heat to molten metal pool [35]. The temperature of metal at slag/metal interface increases correspondingly.

As shown in the right half of subfigures of Figure A1, there is still an anticlockwise vortex in slag and a clockwise vortex in metal pool. Compared to the increasing slag temperature, the flow velocities of slag and metal decrease, meanwhile the vortices weaken, and vortex center of slag gradually shifts toward mould wall and top surface of slag pool with increase of filling ratio, which further reduces the uniformity of temperature

distribution. This can be contributed to the reduction and movement of Lorentz force toward the mould wall due to the change of electric current distribution, which weakens the intensity and affected zone of vortex. According to Figures 5 and A1, it can be also observed the filling ratio makes the molten metal pool become shallow, but has small effect on the width of mushy zone. This result agrees with Wang and He's reports that the depth of molten pool decreases with increase of filling ratio when the filling ratio is less than 0.5 [35,36]. It may be because weakening stirring of metal pool slows the renovation of temperature and the lower temperature gradient.

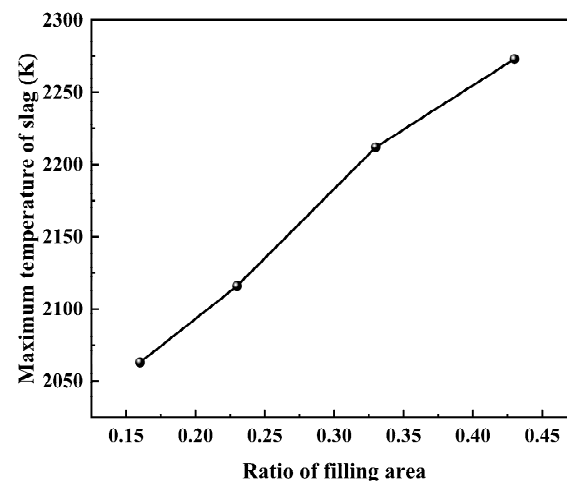


Figure 4. Effect of filling ratio on maximum slag temperature.

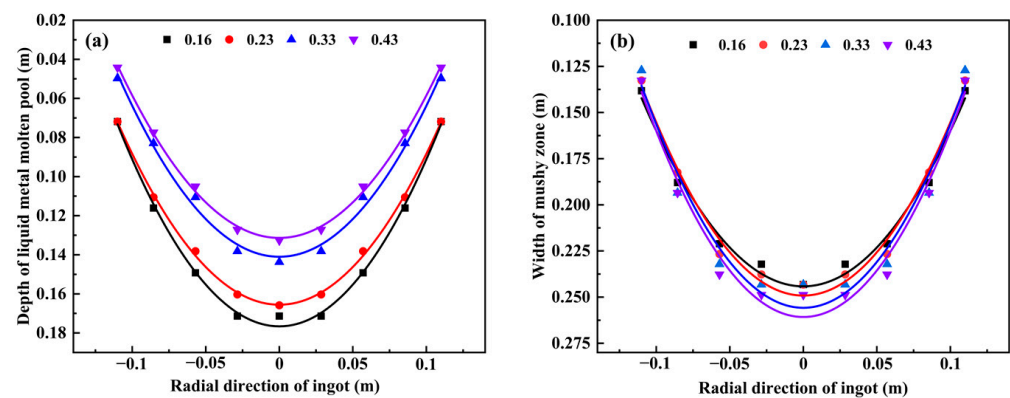


Figure 5. Change of metal pool depth (a) and mushy zone width (b) along radial direction with varying filling ratios.

3.1.3. Effect of Slag Thickness on Temperature and Flow Field

Figure A2a–d displays the evolution of temperature field and flow field of slag pool and metal pool. As shown in the left half of each subfigure, both the high temperature zones of slag pool and metal pool shrink with the increase of slag thickness from 0.08 m to 0.14 m. The highest slag temperature decreases to about 2050 K from about 2160 K according to Figure 6. During ESR process, Joule heating is generated in the slag, increase of slag thickness is beneficial for generation of more Joule heating. While in the meantime, the increase of slag thickness also enlarges the contact area between slag and water-cooling mould wall, more heat is transferred out from slag pool. It seems the heat transfer toward mould wall dominates the result under the competition of heat generation and heat transfer for slag pool. According to Figures 7 and A2, the depth of metal pool increases firstly then has a decreasing tendency despite of the small variation amplitude. This may be because the heat transfer from slag into metal pool decreases with increasing slag thickness and

decreasing slag temperature. When the heat brought is less than that taken through cooling, the metal pool depth begins to decrease.

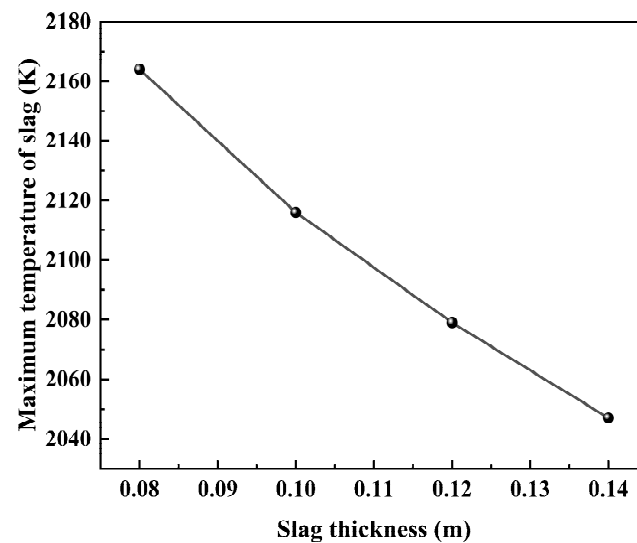


Figure 6. Effect of slag thickness on maximum slag temperature.

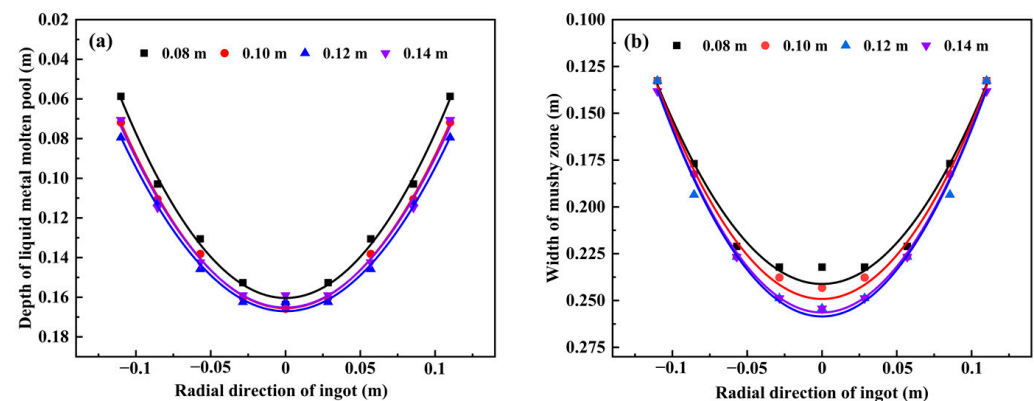


Figure 7. Change of metal pool depth (a) and mushy zone width (b) along radial direction with varying slag thickness.

3.2. Solidification Structure

3.2.1. Effect of Melting Rate on Solidification Structure

LST is the required time of the steel for completing solidification, which reveals the residence time of steel in mushy zone. LST is always employed as a critical criterion to evaluate the solidification structure of steel. Figure 8 demonstrates the LST distribution of the solidified ESR ingot with varying melting rates. It can be seen from a single figure that the bottom and circumference of the ESR ingot shows a shorter LST, but the LST becomes longer when closing to the center of the ingot from both the lateral wall and the bottom. This can be contributed to the change of cooling effect of water-cooling mould wall and basement. The heat transfer during ESR solidification is mainly through water-cooling mould wall and basement. The cooling intensity is higher in the region near the mould lateral wall and basement. With the solidification of ingot and rise of molten pool level, the cooling rate decreases gradually. According to the Equation (27), LST increases correspondingly.

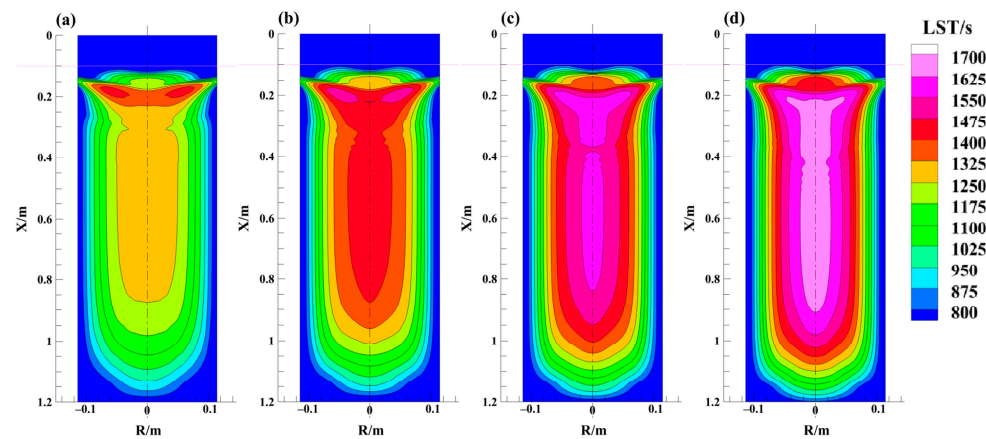


Figure 8. LST distribution at varying melting rate: (a) 90 kg/h, (b) 120 kg/h, (c) 150 kg/h and (d) 180 kg/h.

As shown in Figure 8, the increase of melting rate from 90 kg/h to 180 kg/h also causes obvious influence on LST distribution of ESR ingot. The influence on LST is especially obvious in the center of ESR ingot. It can be seen clearly LST in the center grows greatly. The detailed change of LST can be found in Figure 9, which presents LST change along radial direction at half height of solidified ESR ingot. As shown in Figure 9, the change of LST presents a parabola shape along the diameter. In the lateral surface zone of ingot, it has a slightly shorter LST of about 600 s at higher melting rate compared to about 700 s at a lowest melting rate 90 kg/h. However, as it approaches the ingot center, the LST becomes longer at higher melting rate. A LST difference of about 450 s in the center can be found when comparing the lowest and highest melting rate. Rise of melting rate can increase the solidification rate R , the width of mushy zone also increases while the temperature gradient G_L decreases correspondingly [37,38]. According to the Equation (27), if solidification rate is dominant, increase of melting rate can increase the cooling rate $G_L \cdot R$, so LST decreases. When temperature gradient G_L is dominant, increase of melting rate decreases the cooling rate $G_L \cdot R$, thus LST increases. Obviously, on the ingot surface at higher melting rate, solidification rate is in dominant position, then the dominant becomes temperature gradient when being away from surface. According to the above, LST increases with increase of melting rate in the current study range in most part of ESR ingot.

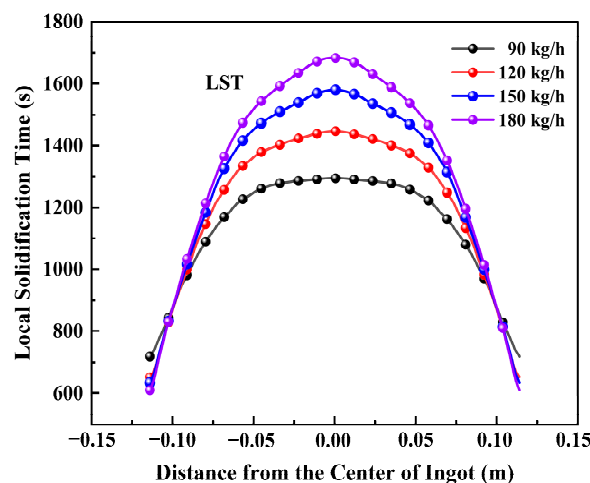


Figure 9. Change of LST along radial direction with varying melting rate.

PDAS and SDAS are the most intuitive evaluation parameters of solidification structure. Figures 10 and 11 demonstrate the distributions of PDAS and SDAS. It can be seen from a single figure that the PDAS and SDAS in the bottom and circumference zone of the

ESR ingot are also small due to intensive cooling around bottom and lateral surface. Then they grow gradually as closing to the ESR ingot center because of weakening cooling. An unusual increase of PDAS and SDAS in the head zone of ESR ingot can be noticed. It may be caused by the feeding in the late ESR stage. In this period, the molten pool shrinks with the rapid drop of melting rate, meanwhile the top surface solidifies rapidly but the lower metal has no enough time to supplement.

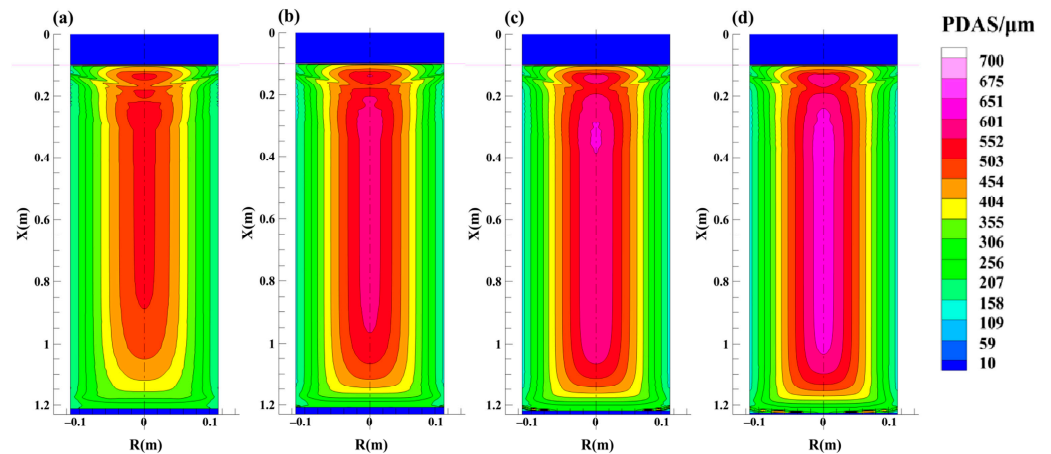


Figure 10. Distribution of PDAS at varying melting rate: (a) 90 kg/h, (b) 120 kg/h, (c) 150 kg/h and (d) 180 kg/h.

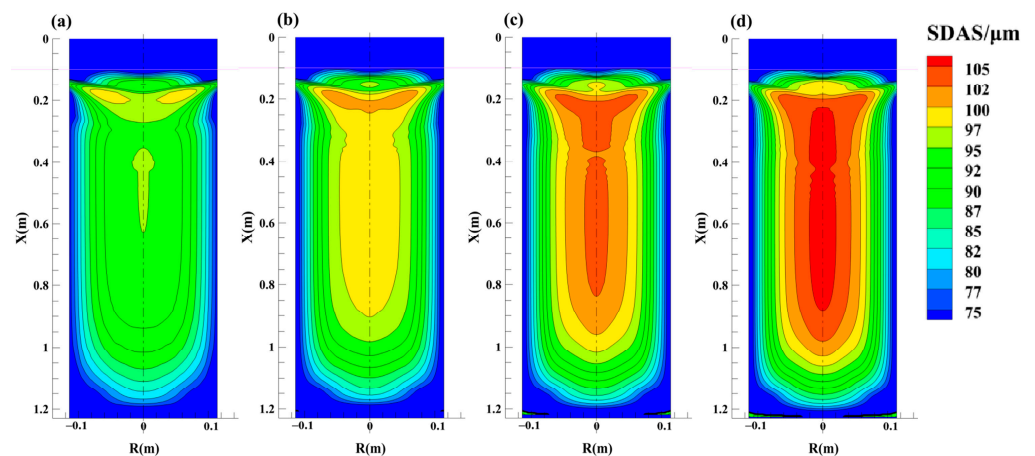


Figure 11. Distribution of SDAS at varying melting rate: (a) 90 kg/h, (b) 120 kg/h, (c) 150 kg/h and (d) 180 kg/h.

It can be also found the distribution zones of large PDAS and SDAS enlarge gradually with the increase of melting rate from 90 kg/h to 180 kg/h. In order to specifically clarify the change of solidification structure with melting rate, PDAS and SDAS of solidified ESR ingot are taken at half height along radical direction and then are illustrated in Figure 12. The center zone presents largest PDAS and SDAS. Moreover, the highest melting rate causes largest PDAS and SDAS in the center zone, they have a respective increase of about 100 μm and 12 μm with increase of melting rate from 90 kg/h to 180 kg/h. It is not difficult to notice a similar change tendency of PDAS and SDAS to LST shown in Figure 9. Shi et al. [39] reported the similar results based on experimental study. He found SDAS of the ingot increased with the increase in the melting rates of electroslag rapid remelting (ESRR), and contributed it to the increase in the LST. Flemings et al. [40] associated dendrite arm spacing to LST through Equation (34).

$$\log \lambda = k_1 + k_2 \log LST \quad (34)$$

where λ is dendrite arm spacing, k_1 and k_2 are constants related to steel compositions. A linear relationship between dendrite arm spacing and LST is expressed through the equation. This also agrees with the consistent change of PDAS and SDAS with respect to LST shown in Figures 9–12. According to Flemings’s solidification theory [40], dendrite arm spacing depends on the heat transfer condition. According to Figures 1 and 3, a lower temperature gradient can be found due to wider mushy zone at higher melting rate. High melting rate results in the low cooling rate with temperature gradient being dominant. Due to the long LST, the solidification of steel inclines to equilibrium solidification, thus the nucleation and growth of dendrites become slow, eventually the solidification structure is coarse.

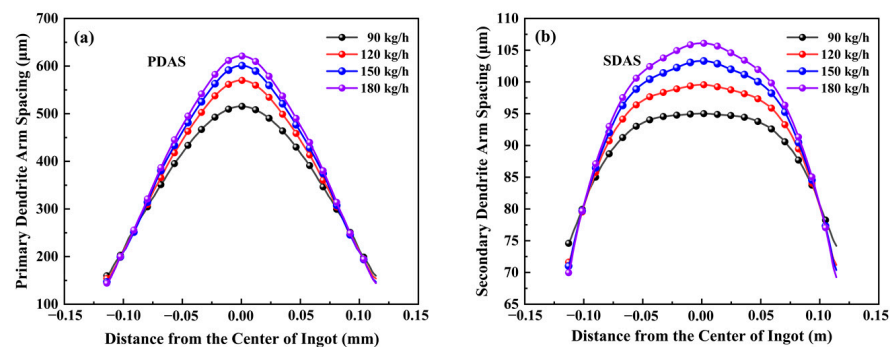


Figure 12. Change of PDAS (a) and SDAS (b) along radical direction with varying melting rate.

3.2.2. Effect of Filling Ratio on Solidification Structure

Figure A3 illustrates the LST distribution in the solidified ESR ingot. It can be seen the area with long LST enlarges gradually with increase of filling ratio. A clear LST distribution along radical direction at the half height of the ESR is plotted in Figure 13. The LST increases from the intensive-cooling edge to the weak-cooling center. At the same radical position, the LST presents an increase with increase of filling ratio but the increasement is small. Figures A4 and A5 illustrate the PDAS and SDAS distribution with rise of filling ratio. It seems PDAS doesn’t present obvious change but SDAS in the center has an increase. More intuitive change can be observed from Figure 14, which depicts evolution of PADS and SDAS along the diameter at the half height of ESR ingot. Consistently, there is little change of PDAS, the largest increasement of SDAS is only within 5μm with the increase of filling ratio from 0.16 to 0.43. As discussed above, there is a linear relationship between dendrite arm spacing and LST. The little change of LST in Figure 13 also indicates the little change of dendrite arm spacing here. The essential factor can be contributed to the steady temperature gradient, which dominates the change of cooling rate, and then the LST and dendrite arm spacing in the ESR ingot.

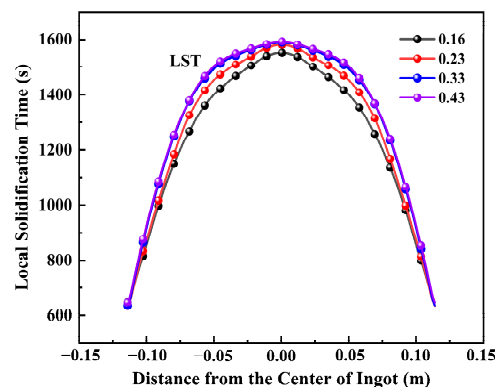


Figure 13. Change of LST along radical direction with varying filling ratio.

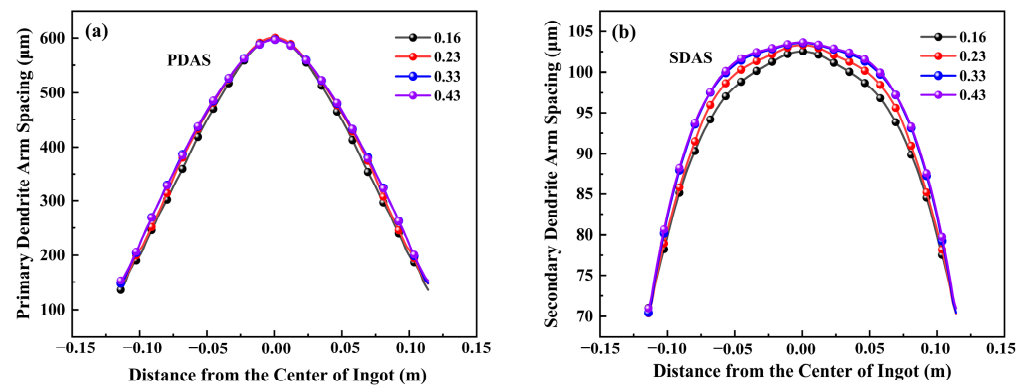


Figure 14. Change of PDAS (a) and SDAS (b) along radical direction with varying filling ratio.

3.2.3. Effect of Slag Thickness on Solidification Structure

As shown in Figure A6, LST presents an increasing tendency and then a slight decrease revealed by the reduced distribution area of long LST. The LST distribution along radical direction at half height of ESR ingot is displayed in Figure 15 in details. LST increases as closing to the center and approaches the longest value at the center. LST at center presents an increase firstly when slag thickness is not more than 0.12 m and then descends slightly. This is consistent with the change of metal pool depth presented in Figure 7. Cooling is slow in the deep molten pool, so the LST becomes long correspondingly. Figures A7 and A8 display PDAS and SDAS distribution in the solidified ESR ingot. An increasing tendency of PDAS and SDAS can be observed with increase of slag thickness. But the slight reduction of area with high PDAS and SDAS is also noticed when the slag thickness exceeds 0.12 m. Figure 16 plots the specific change of PDAS and SDAS at half height of ESR ingot. The same evolution rule of PDAS and SDAS can be found. There is almost no difference in PDAS and SDAS for the structure size in the zone out of the midradius of the ingot for varying slag thicknesses. PDAS and SDAS in the center increase firstly and then has a slight decreasing tendency, which agrees with change of LST as shown in Figure 15. The slag thickness changes the heat in the metal pool, subsequently the metal pool depth changes LST. Different LST allows more or less time for nucleation and growth of grains. Eventually, the change result is revealed by dendrite arm spacing.

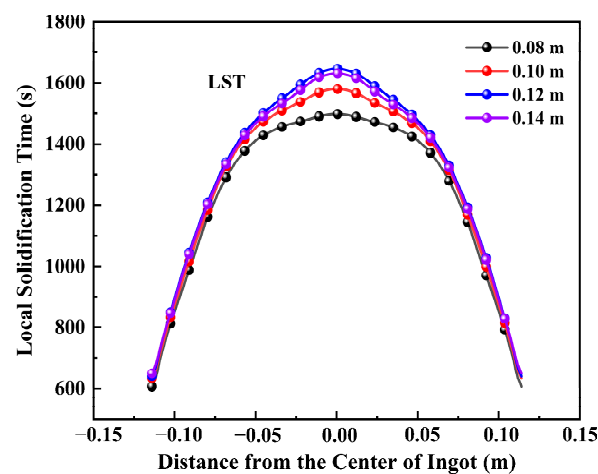


Figure 15. Change of LST along radical direction with varying slag thickness.

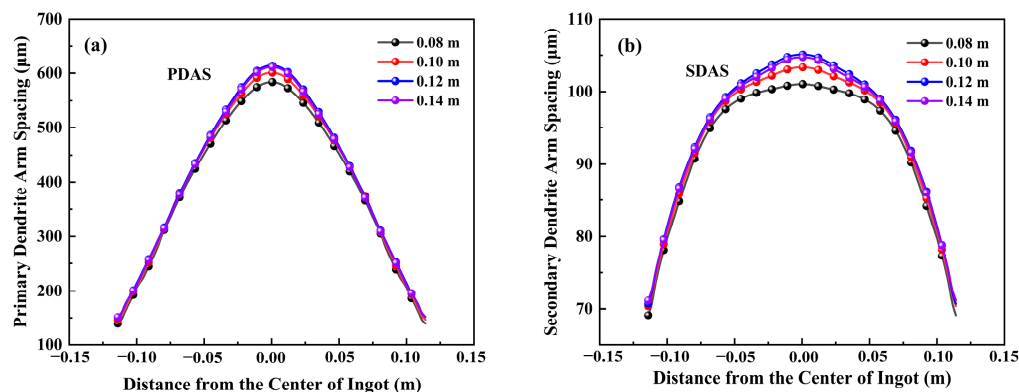


Figure 16. Change of PDAS (a) and SDAS (b) along radical direction with varying slag thickness.

3.3. Macrosegregation

3.3.1. Effect of Melting Rate on Macrosegregation

Coarse primary carbide is a critical factor deteriorating the quality of high carbon steels, which is difficult to be removed through subsequent treatment process. In the high carbon martensitic stainless steels in this study, Cr_7C_3 is primary carbides [41]. The macrosegregation of C and Cr in the steel will enhance the generation of primary carbides in the high carbon martensitic stainless steels. Figures 17 and 18 demonstrate the distributions of C and Cr in the solidified ESR ingot. It can be seen the C and Cr concentrations are high in the center but low at the periphery. With the increase of melting rate, the C and Cr concentrations in the center increases gradually and the area with high concentration enlarges along radical and axial directions. Figure 19 further illustrates the segregation index of C and Cr along vertical centerline of ESR ingot. The segregation index is defined as Equation (35).

$$S = \frac{c - c_0}{c_0} \times 100\% \quad (35)$$

where c is concentration of C or Cr in the solidified ESR ingot, c_0 is initial concentration of C or Cr in the electrode. It can be seen clearly from Figure 19 the segregation index of C and Cr illustrates similar change tendency from head to bottom of ESR ingot. A negative segregation index due to intensive cooling of bottom water tank can be found, whereas it quickly transforms into positive segregation toward the head zone, where molten metal solidifies slowly. In the final stage of ESR solidification, the solidification shrinkage of ESR ingot exacerbates the segregation due to descending slag temperature and weak heat insulation. It can be seen a sudden increase of segregation in the range of 0–0.2 m from Figures 17–19. For a typical height range of 0.2–1.0 m, the segregation indexes of C and Cr are positive and increases with increasing melting rate. The effect of melting rate on C and Cr segregation shows Liu [9] and Wang [10] reported the similar effect of melting rate characterized by current on enhancement of Cr and Ni segregation based on laboratory-scale experiments. Further, Wang [14,32] presented the similar change tendency of local carbon content along centerline based on the simulation and experiment. All these studies verify the reliability of the present simulation results. As discussed above, high melting rate would deepen the molten metal pool and thus the closed mushy zone would become broader due to the crossing primary dendrite arms. The partition coefficient between solid and liquid phase of C is far less than unity, the value of Cr is close to unity but still less than unity in the high alloy steels [42]. During ESR solidification process, C and Cr are ejected from solid to liquid incessantly. With the action of thermal buoyancy, the solute-rich and hotter metal at the solidification front floats due to the driving of clockwise vortex discussed above. High melting rate enhances the clockwise vortex, and thus enhances C and Cr segregation. Cr has higher partition coefficient than C, so its segregation index is lower. Moreover, another effect of melting rate is that it decreases the temperature gradient, this is not beneficial for stratification solidification to block the floatation of solute-rich

liquid. The large SDAS and long LST under low temperature gradient prolong the diffusion time of solute elements, which exacerbates the segregation.

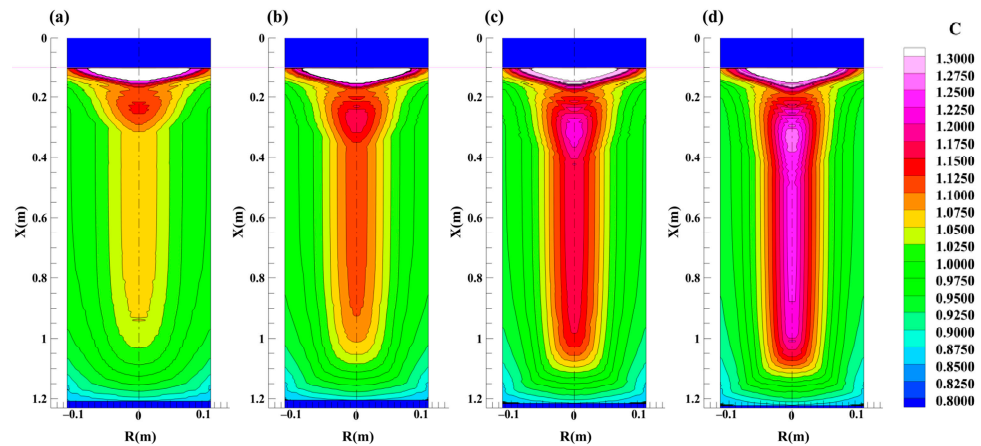


Figure 17. Distribution of C concentration at varying melting rate: (a) 90 kg/h, (b) 120 kg/h, (c) 150 kg/h and (d) 180 kg/h.

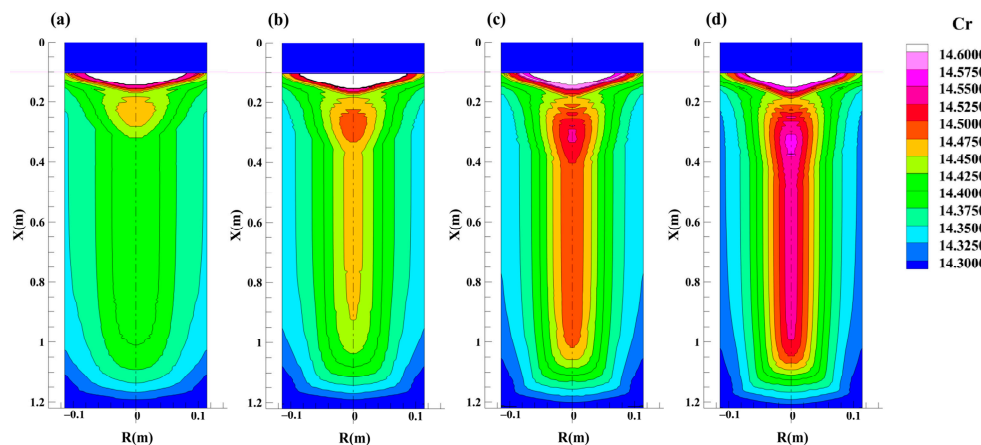


Figure 18. Distribution of Cr concentration at varying melting rate: (a) 90 kg/h, (b) 120 kg/h, (c) 150 kg/h and (d) 180 kg/h.

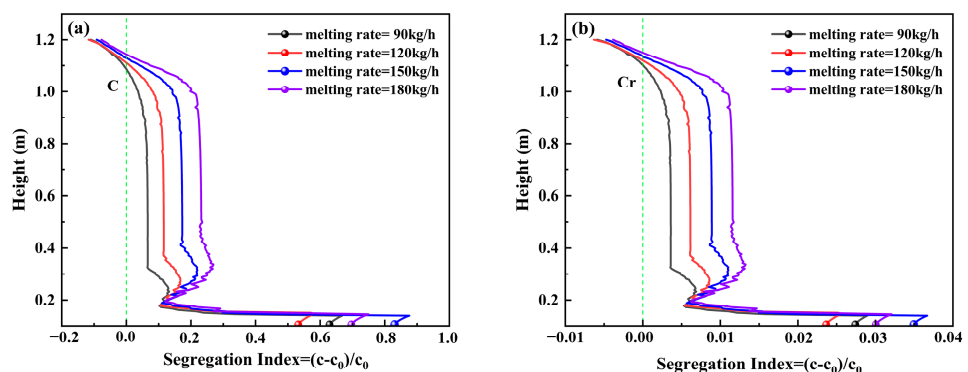


Figure 19. Change of C (a) and Cr (b) centerline segregation index at varying melting rate.

3.3.2. Effect of Filling Ratio on Macrosegregation

Figure 20 illustrates the C and Cr distribution in the ESR ingot. It can be seen there is a slight increase of element contribution in the center with increase of filling ratio. Figure 21 compares the change of centerline segregation index of C and Cr with filling ratio, the centerline segregation index is calculated based on the element concentration

in the centerline of ESR ingot. The overall change tendency of centerline C segregation is consistent with the reported study [14]. The enlarged local figure in Figure 21 makes the comparison clearer. It can be seen a slight increase of the segregation index, which agrees with the reported effect rule of filling ratio on C segregation in the middle zone of 201 stainless steel ESR ingot [14]. The change of segregation index is also consistent with the change of SDAS. As discussed above, this is because small SDAS helps restrain the element segregation because it shortens the diffusion distance of elements and thus restricts and disperses them in a small microcell.

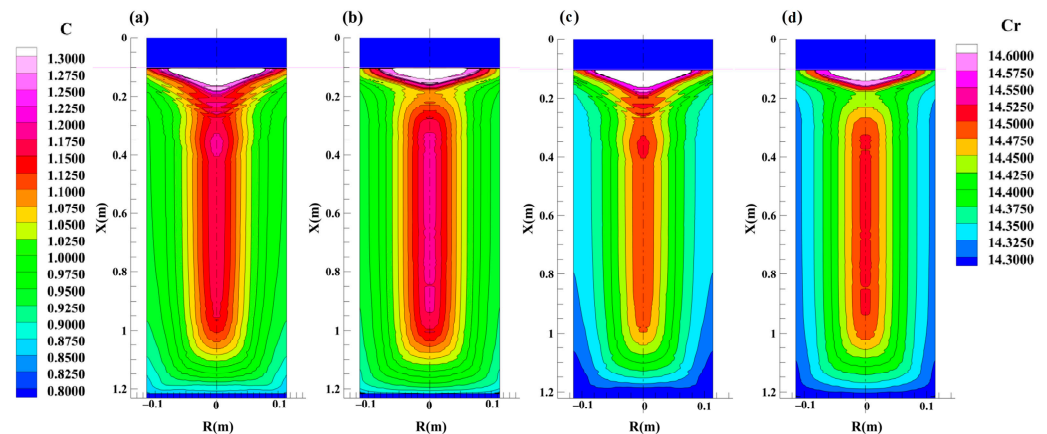


Figure 20. Distribution of C and Cr concentration with varying filling ratio: (a) C concentration, 0.16, (b) C concentration, 0.43, (c) Cr concentration, 0.16 and (d) Cr concentration, 0.43.

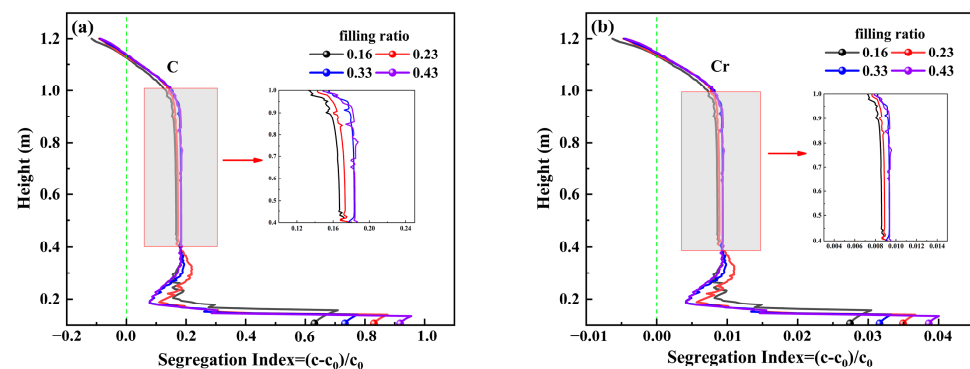


Figure 21. Change of C (a) and Cr (b) centerline segregation index with varying filling ratio.

3.3.3. Effect of Slag Thickness on Macrosegregation

Figure 22 displays the C and Cr concentration in the ESR ingot. An area reduction of high concentration zone can be found from low slag thickness to high slag thickness. The centerline segregation index of C and Cr shown in Figure 23 illustrates the change in detail. Due to the shrinkage in the center as shown in Figure 23a,c, the segregation index presents an abrupt change. Take the segregation index in the upper half part of ESR ingot for example, the segregation index increases firstly and then decreases with increases of slag thickness. In combination with the previous discussion on the change of dendrite arm spacing with slag thickness, similar change of dendrite arm spacing with segregation index due to slag thickness indicates it is a critical factor affecting the segregation index.

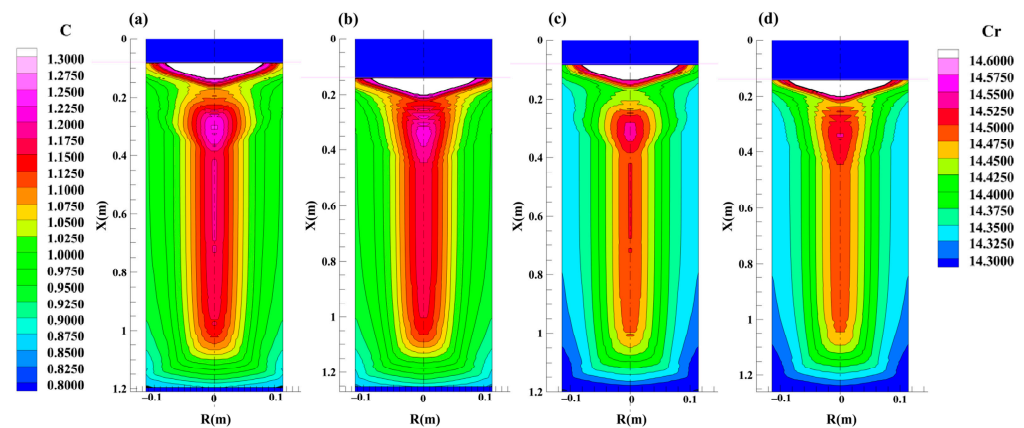


Figure 22. Distribution of C and Cr concentration with varying slag thickness: (a) C concentration, 0.08 m, (b) C concentration, 0.14 m, (c) Cr concentration, 0.08 m and (d) Cr concentration, 0.14 m.

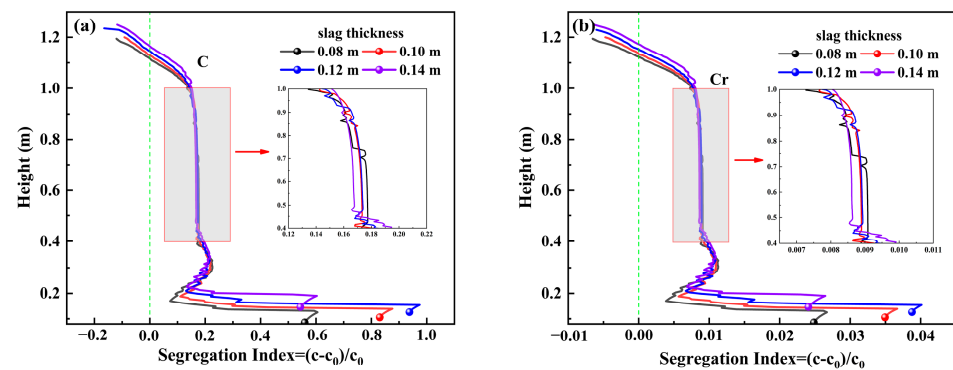


Figure 23. Change of C (a) and Cr (b) centerline segregation index with varying slag thickness.

As discussed above, it can be found the change of melting ratio in the study range causes the most serious impact on the ESR solidification process. Deep molten pool and coarse structures can be viewed in the case of high melting rate. Increase of filling ratio increases the mushy zone width and thus decreases the temperature gradient, meanwhile LST, SDAS and segregation receive a slight rise. An inflection can be observed with respect to the molten pool depth and mushy zone width when increasing slag thickness. LST, SDAS, segregation of C and Cr approach their maximum when the slag thickness increases to 0.12 m. To sum up, a low melting rate less than 120 kg/h, a filling ratio of about 0.23–0.33 and a slag thickness of 0.08–0.10 m are suggested for ESR process of high carbon stainless steels in this study through synthetical consideration with the whole ESR solidification process.

4. Conclusions

1. As the increase of melting rate, the molten metal pool depth increases, the temperature gradient and highest slag temperature decrease, the anticlockwise vortex in the slag and the clockwise vortex in the metal pool enlarge. LST, PDAS and SDAS increase greatly, meanwhile the segregation of C and Cr deteriorates with increasing melting rate.
2. Increase of filling ratio reduces the metal pool depth within a small range but increases the mushy zone width, maximum slag temperature and metal temperature at slag/metal interface. A mild increase of LST and SDAS is observed but the change of PDAS is little with rise of filling ratio. In the same time, centerline segregation of C and Cr increases marginally with increasing filling ratio.
3. The metal pool depth increases firstly and then decrease slightly with rising slag thickness. The flow intensity in the vortex center weakens and the highest slag

temperature decreases as rise of slag thickness. LST, PDAS, SDAS, segregation of C and Cr present similar change tendency with metal pool depth as the increase of slag thickness.

4. Through a comprehensive consideration on temperature and flow field, metal pool profile, solidification structure and element segregation, a low melting rate less than 120 kg/h, a filling ratio of about 0.23–0.33 and a slag thickness of 0.08–0.10 m are suggested for ESR process of high carbon stainless steels in this study.

Author Contributions: Conceptualization, W.Y. and G.Z.; methodology, X.L. and G.Z.; software, G.Z.; formal analysis, X.L. and W.Y.; investigation, X.L. and G.Z.; data curation, X.L., G.Z. and Y.S.; writing—original draft preparation, X.L.; writing—review and editing, W.Y.; visualization, X.L. and Y.S.; supervision, W.Y. and J.L.; funding acquisition, W.Y. All authors have read and agreed to the published version of the manuscript.

Funding: This research was funded by the National Natural Science Foundation of China, grant number 51904022.

Data Availability Statement: Not applicable.

Conflicts of Interest: The authors declare no conflict of interest.

List of Symbols

| | |
|-------------------------|--|
| ∇ | Vector operator nabla (1/m) |
| σ | Electrical conductivity (1/($\Omega \cdot m$)) |
| \hat{H}_θ | Complex amplitude of magnetic field intensity (A/m) |
| μ_0 | Vacuum permeability (T·m/A) |
| j | In electrical equations $j = \sqrt{-1}$ |
| ω | Angular frequency (Hz) |
| μ | Dynamic viscosity (Pa·s) |
| \hat{J} | Complex amplitude of current density (A/m ²) |
| F_L | Lorentz force (N/m ³) |
| Conjugate (\hat{B}) | Complex conjugate of magnetic flux density (T) |
| Conjugate (\hat{J}) | Complex conjugate of current density (A/m ²) |
| S_J | Joule heating (W) |
| x | Axial direction |
| \hat{I} | Amplitude of the total current entering the slag (A) |
| r | radius (m) |
| R_{Ingot} | Radius of ESR ingot (m) |
| ρ | Density(kg/m ³) |
| u | Velocity (m/s) |
| g | Gravitational acceleration (m/s ²) |
| P | Pressure (Pa) |
| μ_{eff} | Effective viscosity (Pa·s) |
| h | Sensible enthalpy (J/kg) |
| ΔH | Enthalpy change (J/kg) |
| k_{eff} | Effective thermal conductivity (W/(m·K)) |
| h_{ref} | Reference sensible enthalpy (J/kg) |
| T_{ref} | Reference temperature (K) |
| C_p | Specific heat capacity (J/(kg·K)) |
| L | Latent heat (J/kg) |
| T_{liq}, T_{sol} | Liquidus and solidus temperature (K) |
| λ_1, λ_2 | Primary and secondary dendrite arm spacing (μm) |
| G_L | Temperature gradient (K/m) |
| R | Solidification rate (m/s) |
| \dot{m} | melting rate (kg/h) |
| T_{amb} | Ambient temperature (K) |
| ε_e | Emissivity |
| σ_b | Stefan-Boltzmann constant |

| | |
|---------------|---|
| ε | Turbulence dissipation (m^2/s^3) |
| k | Thermal conductivity ($\text{W}/(\text{m}\cdot\text{K})$) |
| μ_t | Turbulent viscosity ($\text{Pa}\cdot\text{s}$) |
| G | Generation of turbulence kinetic energy due to the mean velocity gradients ($\text{Pa}\cdot\text{s}$) |
| c | Concentration of an alloying element |
| k_t | Turbulent thermal conductivity ($\text{W}/(\text{m}\cdot\text{K})$) |
| Pr_t | Turbulent Prandtl number |
| S | Source term due to mass flux of alloying element ($\text{kg}/(\text{m}^3\cdot\text{s})$) |
| Sc | Schmidt number |

Appendix A

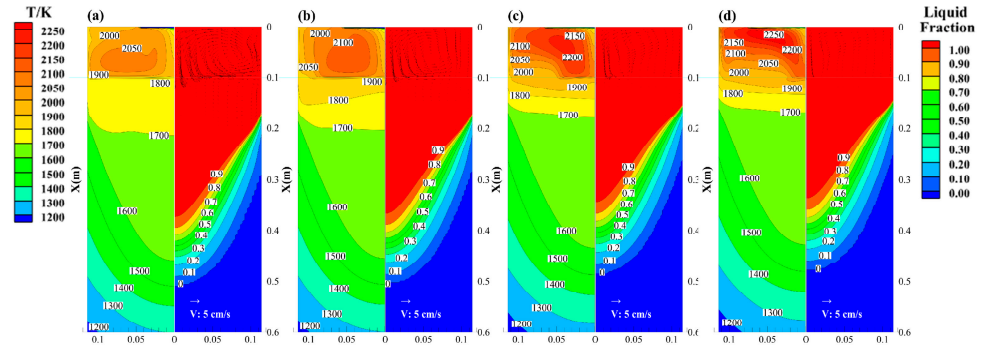


Figure A1. Temperature distribution (left of each figure) and liquid metal volume fraction distribution (right of each figure) as varying filling ratios at end of steady-state: (a) 0.16, (b) 0.23, (c) 0.33 and (d) 0.43.

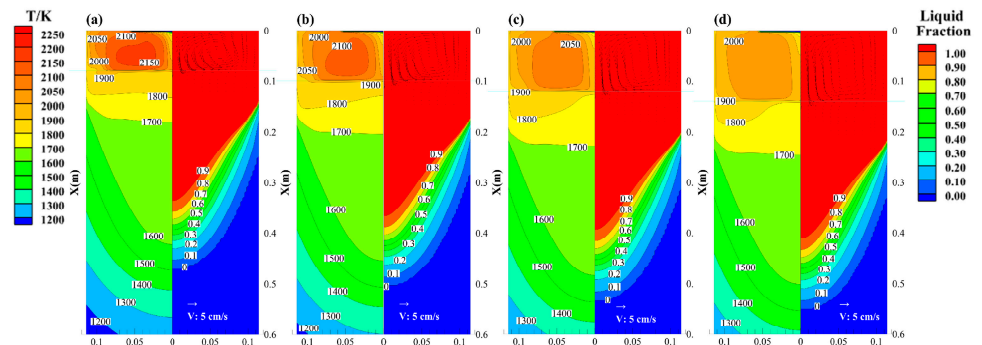


Figure A2. Temperature distribution (left of each figure) and liquid metal volume fraction distribution (right of each figure) as varying slag thickness at end of steady-state: (a) 0.08 m, (b) 0.10 m, (c) 0.12 m and (d) 0.14 m.

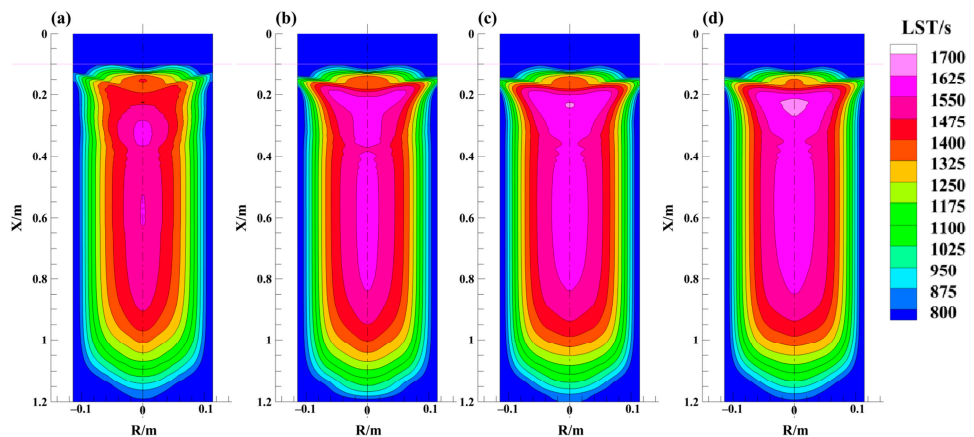


Figure A3. LST distribution with varying filling ratio: (a) 0.16, (b) 0.23, (c) 0.33 and (d) 0.43.

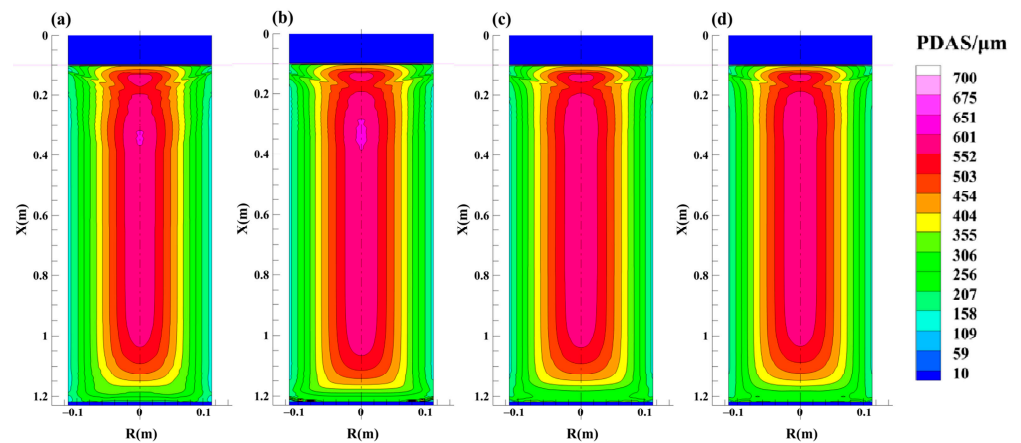


Figure A4. Distribution of PDAS with varying filling ratio: (a) 0.16, (b) 0.23, (c) 0.33 and (d) 0.43.

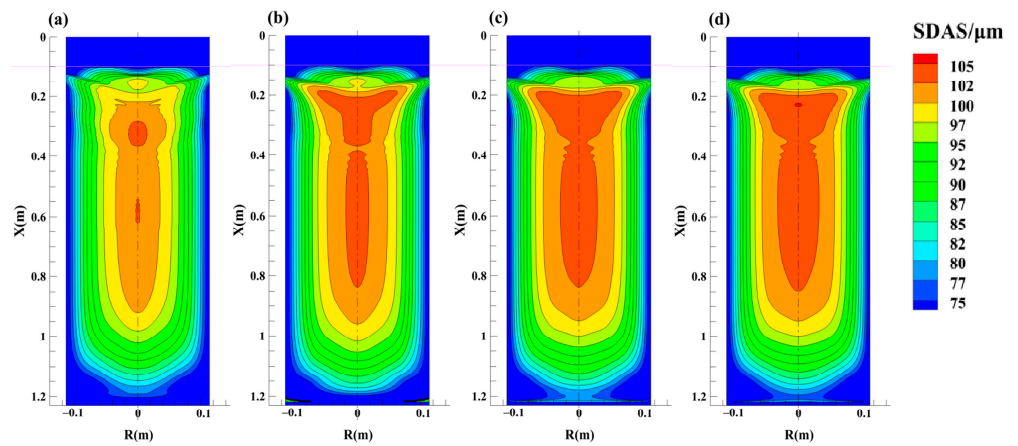


Figure A5. Distribution of SDAS with varying filling ratio: (a) 0.16, (b) 0.23, (c) 0.33 and (d) 0.43.

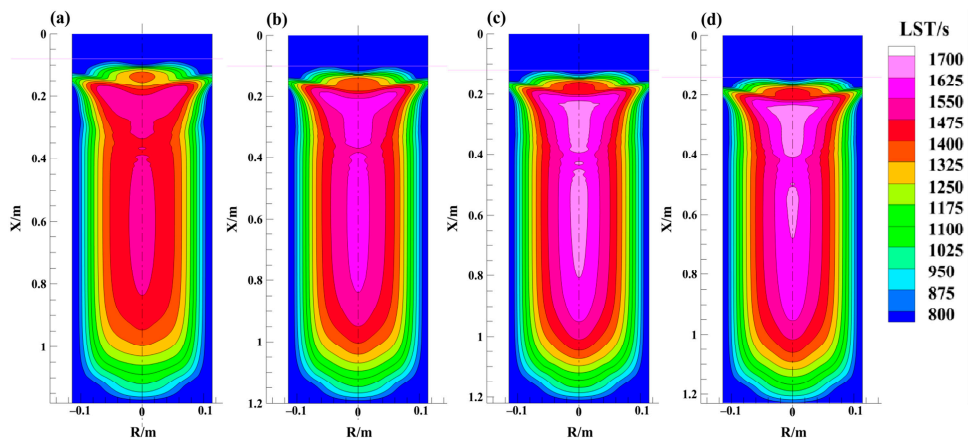


Figure A6. LST distribution with varying slag thickness: (a) 0.08 m, (b) 0.10 m, (c) 0.12 m and (d) 0.14 m.

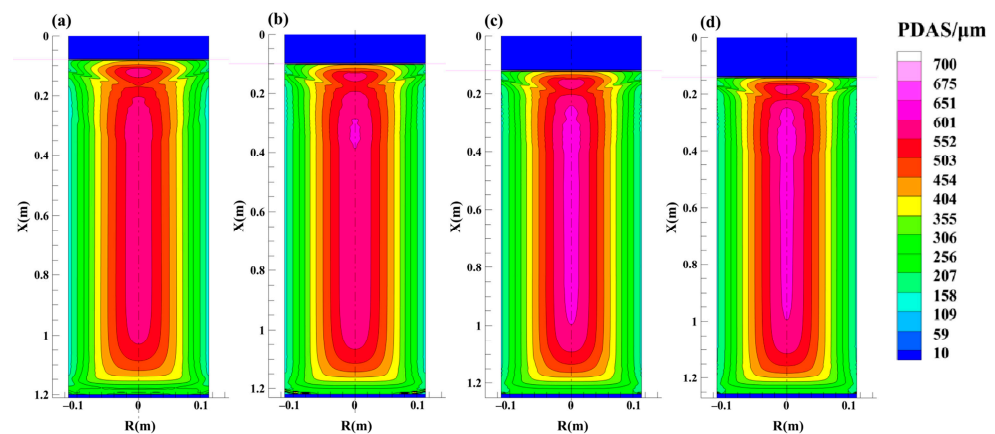


Figure A7. Distribution of PDAS with varying slag thickness: (a) 0.08 m, (b) 0.10 m, (c) 0.12 m and (d) 0.14 m.

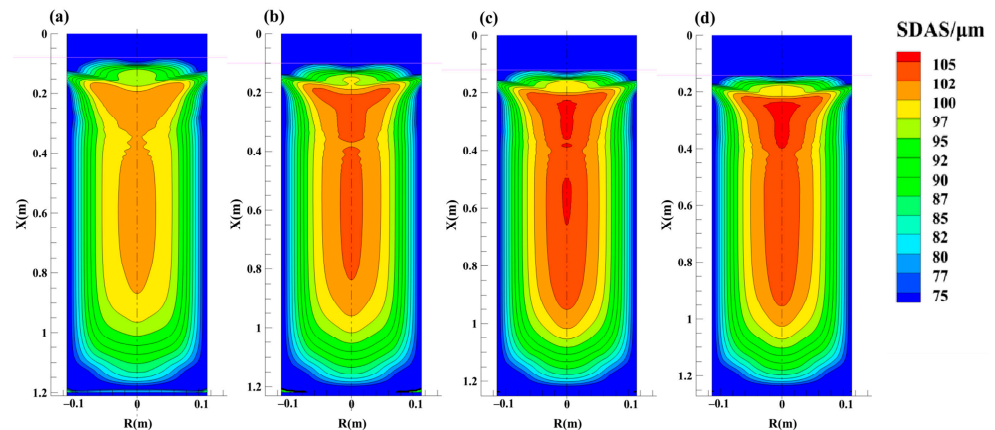


Figure A8. Distribution of SDAS with varying slag thickness: (a) 0.08 m, (b) 0.10 m, (c) 0.12 m and (d) 0.14 m.

References

- Zhuang, W.; Zhou, C. Crack mechanism of high-carbon and chrome martensitic stainless steel. *Baosteel Technol.* **2019**, *3*, 16–19.
- Li, X.; Zhang, Z.; Huo, Z.; Yuan, P. A Method of Continuous Casting of High Carbon Martensitic Stainless Steel. Chinese Patent CN114951579A, 30 August 2022.
- Zhong, H.; Wang, R.; Han, Q. Solidification structure and central segregation of 6Cr13Mo stainless steel under simulated continuous casting conditions. *J. Mater. Res. Technol.* **2022**, *20*, 3408–3419. [[CrossRef](#)]
- Zhang, J.; Li, J.; Shi, C.; Huang, J. Growth and agglomeration behaviors of eutectic M_7C_3 carbide in electroslag remelted martensitic stainless steel. *J. Mater. Res. Technol.* **2021**, *11*, 1490–1505. [[CrossRef](#)]
- Medovar, B.I.; Boyko, G.A. *Electroslag Technology*; Springer: New York, NY, USA, 2013; pp. 155–164.
- Chen, X.; Jiang, Z.; Liu, F. Effect of melt rate on surface quality and solidification structure of Mn18Cr18N hollow ingot during electroslag remelting process. *Steel. Res. Int.* **2017**, *88*, 1600186. [[CrossRef](#)]
- Ridder, S.D.; Reyes, F.C.; Chakravorty, S. Steady state segregation and heat flow in ESR. *Metall. Mater. Trans. B* **1978**, *9*, 415–425. [[CrossRef](#)]
- Wang, Q.; Yan, H.; Ren, N.; Li, B. Effect of slag thickness on macrosegregation and transition zone width of electroslag remelting dual alloy ingot. *JOM* **2016**, *68*, 397–400. [[CrossRef](#)]
- Liu, Y.; Zhang, Z.; Li, G.; Wang, Q.; Wang, L.; Li, B. Effect of current on structure and macrosegregation in dual alloy ingot processed by electroslag remelting. *Metals* **2017**, *7*, 185. [[CrossRef](#)]
- Wang, Q.; Yan, H.; Ren, N.; Li, B. Effect of current on solute transport in electroslag remelting dual alloy ingot. *Appl. Therm. Eng.* **2016**, *101*, 564–567. [[CrossRef](#)]
- Wang, X.; Li, G.; Liu, Y.; Cao, Y.; Wang, F.; Wang, Q. Investigation of primary carbides in a commercial-sized electroslag remelting ingot of H13 steel. *Metals* **2019**, *9*, 1247. [[CrossRef](#)]
- Du, G.; Li, J.; Wang, Z. Control of Carbide Precipitation During Electroslag Remelting-Continuous Rapid Solidification of GCr15 Steel. *Metall. Mater. Trans. B* **2017**, *48*, 2873–2890. [[CrossRef](#)]

13. Wang, Q.; Wang, F.; Li, B.; Tsukihashi, F. A three-dimensional comprehensive model for prediction of macrosegregation in electroslag remelting ingot. *ISIJ Int.* **2015**, *55*, 1010–1016. [[CrossRef](#)]
14. Wang, Q.; Li, B. Numerical investigation on the effect of fill ratio on macrosegregation in electroslag remelting ingot. *Appl. Therm. Eng.* **2015**, *91*, 116–125. [[CrossRef](#)]
15. Li, B.; Wang, F.; Tsukihashi, F. Current, magnetic field and Joule heating in electroslag remelting processes. *ISIJ Int.* **2012**, *52*, 1289–1295. [[CrossRef](#)]
16. Weber, V.; Jardy, A.; Dussoubs, B.; Ablitzer, D.; Rybéron, S.; Schmitt, V.; Hans, S.; Poisson, H. A comprehensive model of the electroslag remelting process: Description and validation. *Metall. Mater. Trans. B* **2009**, *40*, 271–280. [[CrossRef](#)]
17. Huang, X.; Duan, Y.; Liu, Z.; Li, B.; Wang, F. Role of Electrode Rotation on Improvement of Metal Pool Profile in Electroslag Remelting Process. *Metals* **2021**, *11*, 1675. [[CrossRef](#)]
18. Kelkar, K.M.; Patankar, S.V.; Srivatsa, S.K.; Minisandram, R.S.; Evans, D.G.; deBarbadillo, J.J.; Smith, R.H.; Helmink, R.C.; Mitchell, A.; Sizek, H.A. Computational modeling of the electroslag remelting (ESR) process used for the production of ingots of high-performance alloys. In Proceedings of the 2013 International Symposium on Liquid Metal Processing and Casting, Pittsburgh, OR, USA, 22–25 September 2013.
19. Kelkar, K.; Patankar, S.; Mitchell, A.; Kanou, O.; Fukada, N.; Suzuki, K. Computational modeling of the vacuum arc remelting (VAR) process used for the production of ingots of titanium alloys. In Proceedings of the 11th World Conference on Titanium, Kyoto, Japan, 3–7 June 2007.
20. Kelkar, K.M.; O’Connell, C.J. A computational model of the electroslag remelting (ESR) process and its application to an industrial process for a large diameter superalloy ingot. In Proceedings of the 9th International Symposium on Superalloy 718 & Derivatives, Pittsburgh, OR, USA, 3–6 June 2018.
21. Kelkar, K.M.; Patankar, S.V.; Mitchell, A.; Minisandram, R.S.; Patel, A.D. Computational analysis of the vacuum arc remelting (VAR) and electroslag remelting (ESR) processes. *ASM Handbook* **2010**, *22*, 196–213.
22. Fezi, K.; Yanke, J.; Krane, M.J.M. Macrosegregation during electroslag remelting of alloy 625. *Metall. Mater. Trans. B* **2015**, *46*, 766–779. [[CrossRef](#)]
23. Zu, Y.; Yan, Y. A numerical investigation of electrohydrodynamic (EHD) effects on bubble deformation under pseudo-nucleate boiling conditions. *Int. J. Heat Fluid Fl.* **2009**, *30*, 761–767. [[CrossRef](#)]
24. Jardy, A.; Ablitzer, D.; Wadier, J.F. Magnetohydrdynamic and thermal behavior of electroslag remelting slags. *Metall. Mater. Trans. B* **1991**, *22*, 111–120. [[CrossRef](#)]
25. Launder, B.E.; Spalding, D.B. The numerical computation of turbulent flow. *Comp. Meth. in Appl. Mech. and Eng.* **1974**, *3*, 269–289. [[CrossRef](#)]
26. Cui, J.; Li, B.; Liu, Z.; Qi, F.; Zhang, B.; Zhang, J. Numerical investigation of segregation evolution during the vacuum arc remelting process of Ni-based superalloy ingots. *Metals* **2021**, *11*, 2046. [[CrossRef](#)]
27. Flemings, M.C. *Solidification Processing*; McGraw-Hill Book, Co.: New York, NY, USA, 1974; p. 148.
28. Kurz, W.; Fisher, D.J. *Fundamentals of Solidification*; Trans Tech Publications Ltd.: Aedermannsdorf, Switzerland, 1992; pp. 123–125.
29. Dilawari, A.H.; Szekely, J. Heat transfer and fluid flow phenomena in electroslag refining. *Metall. Mater. Trans. B* **1978**, *9*, 77–87. [[CrossRef](#)]
30. Dong, Y.; Jiang, Z.; Fan, J.; Cao, Y.; Hou, D.; Cao, H. Comprehensive Mathematical Model for Simulating Electroslag Remelting. *Metall. Mater. Trans. B* **2016**, *47*, 1475–1488. [[CrossRef](#)]
31. Wang, Q.; He, Z.; Li, B.; Tsukihashi, F. A general coupled mathematical model of electromagnetic phenomena, two phase flow, and heat transfer in electroslag remelting process including conducting in the mold. *Metall. Mater. Trans. B* **2014**, *45*, 2425–2441. [[CrossRef](#)]
32. Wang, Q.; He, Z.; Li, G.; Li, B. Numerical investigation on species transport in electroslag remelting dual alloy ingot. *Appl. Therm. Eng.* **2016**, *103*, 419–427. [[CrossRef](#)]
33. Hoyle, G. *Electroslag Processes: Principles and Practice*; Applied Science Publishers Ltd.: London, UK, 1983; p. 111.
34. Nastac, L.; Sundarraj, S.; Yu, K.; Pang, Y. The stochastic modeling of solidification structures in alloy 718 remelt ingots. *JOM* **1998**, *3*, 30–35. [[CrossRef](#)]
35. Wang, F.; Xiong, Y.; Li, B. Impact of fill ratio on temperature profile and metal bath configuration in electroslag remelting process with vibrating electrode. *Steel Res. Int.* **2019**, *90*, 1800092. [[CrossRef](#)]
36. He, Z.; Liu, Y.; Liu, S.; Liu, Z.; Li, B. Numerical simulation of effect of electrode filling ratio on electroslag remelting process. *Special Steel* **2014**, *35*, 16–19.
37. Sjöberg, B.; Cedneriund, A.; Engström, C.H. The influence of the ESR melting rate and ingot size on some important properties of tool steels. In Proceedings of the 4th International Symposium on Electroslag Remelting Processes, Tokyo, Japan, 7–8 June 1973.
38. Dong, Y.; Jiang, Z.; Li, Z. Mathematical model for electroslag remelting process. *J. Iron. Steel Res. Int.* **2007**, *14*, 7–30. [[CrossRef](#)]
39. Shi, C.; Zheng, X.; Yang, Z.; Lan, P.; Li, J.; Jiang, F. Effect of Melting Rate of Electroslag Rapid Remelting on the Microstructure and Carbides in a Hot Work Tool Steel. *Met. Mater. Int.* **2021**, *27*, 3603–3616. [[CrossRef](#)]
40. Flemings, M.C. *Solidification Processing*; Metallurgical Industry Press: Beijing, China, 1981; p. 104.

41. Sun, C.; Li, J.; Zhang, J.; Yan, W.; Li, S. Formation and evolution of primary carbides in high-carbon martensitic stainless steel. *J. Iron Steel Res. Int.* 2022; *in press*. [[CrossRef](#)]
42. Morita, Z.; Tanaka, T. Thermodynamics on the equilibrium distribution coefficients of solute elements between solid and liquid phases in iron alloys. *Tetsu Hagane* **1988**, *74*, 1210–1218. [[CrossRef](#)] [[PubMed](#)]

Disclaimer/Publisher's Note: The statements, opinions and data contained in all publications are solely those of the individual author(s) and contributor(s) and not of MDPI and/or the editor(s). MDPI and/or the editor(s) disclaim responsibility for any injury to people or property resulting from any ideas, methods, instructions or products referred to in the content.